This is an open access article published under an ACS AuthorChoice License, which permits copying and redistribution of the article or any adaptations for non-commercial purposes.

ACS APPLIED MATERIALS & INTERFACES

www.acsami.org Research Article

Electron Transport across Vertical Silicon/MoS_2/Graphene Heterostructures: Towards Efficient Emitter Diodes for Graphene Base Hot Electron Transistors

Melkamu Belete, Olof Engström, Sam Vaziri, Gunther Lippert, Mindaugas Lukosius, Satender Kataria,* and Max C. Lemme*

Cite This: *ACS Appl. Mater. Interfaces* 2020, 12, 9656−9663 Read Online

ACCESS | Metrics & More | Article Recommendations | Supporting Information

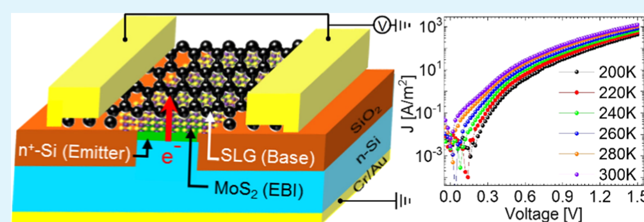

ABSTRACT: Heterostructures comprising silicon, molybdenum disulfide (MoS_2), and graphene are investigated with respect to the vertical current conduction mechanism. The measured current−voltage ($I-V$) characteristics exhibit temperature-dependent asymmetric current, indicating thermally activated charge carrier transport. The data are compared and fitted to a current transport model that confirms thermionic emission as the responsible transport mechanism across devices. Theoretical calculations in combination with the experimental data suggest that the heterojunction barrier from Si to MoS_2 is linearly temperature-dependent for T = 200−300 K with a positive temperature coefficient. The temperature dependence may be attributed to a change in band gap difference between Si and MoS_2, strain at the Si/MoS_2 interface, or different electron effective masses in Si and MoS_2, leading to a possible entropy change stemming from variation in density of states as electrons move from Si to MoS_2. The low barrier formed between Si and MoS_2 and the resultant thermionic emission demonstrated here make the present devices potential candidates as the emitter diode of graphene base hot electron transistors for future high-speed electronics.

KEYWORDS: *2D materials, TMD, MoS_2, graphene, vertical heterostructures, electron transport, charge carrier transport, thermionic emission*

I. INTRODUCTION

Hot electron transistors (HETs) have been proposed first by Mead in the 1960s as potential high-performance electron devices.[1] Such transistors rely on vertical device structures with cross-plane transport of high-energy electrons (hot electrons). The first HETs comprised a metal emitter, a base, and a collector, isolated from each other by thin oxide layers. The cutoff frequency in these devices is limited by the base transit time. While thinning down the metallic base mitigates this issue, it increases the base resistance, resulting in high RC delay and self-bias crowding. Graphene base transistors (GBTs), where graphene replaces the metallic base electrodes, have been proposed to exploit the high conductivity and ultrathinness of graphene as the base material in HETs to minimize the base transit time and achieve high cutoff frequencies.[2−10] Although experimental demonstration of GBTs is limited to direct current (DC) characteristics, simulations clearly show that the performance greatly depends on the properties of the injection barrier that isolates the emitter and the base. In fact, high-level on-state collector currents (I_{ON}) can be achieved only by choosing injection barriers that form relatively small conduction band (CB) offsets with respect to the emitter.[11−14] Thus, vertical heterostructures with low barriers, similar to compound semiconductor structures investigated by Heiblum et al.,[15,16] have been proposed to enable high-frequency performance reaching (theoretically) the THz regime.[11−13] An illustration of the structure and operation of a GBT with molybdenum disulfide (MoS_2) as the emission barrier is shown in Figure S1.

The two-dimensional (2D) material MoS_2 is one of the most explored 2D transition-metal dichalcogenides due to its electronic properties that have made it a potential choice for future nanoelectronic, optoelectronic, and flexible electronic devices.[5,17−23] Unlike graphene, MoS_2 is known for its intrinsic semiconducting behavior and sizeable band gap (i.e., 1.3 eV in bulk and as high as 2.16 eV in monolayer).[21,24] According to theory, MoS_2 can provide a desirable low barrier for carrier injection in GBTs in combination with highly doped silicon (Si) emitters and graphene base electrodes. The electron affinity of bulk MoS_2 is reported to be 4 eV,[25,26] indicating the small band offset it would make with respect to Si that has an electron affinity of 4.05 eV. Also, based on the literature values

Received: December 2, 2019
Accepted: January 30, 2020
Published: January 30, 2020

Downloaded via LEIBNIZ UNIVERSITAET HANNOVER on August 26, 2021 at 08:14:40 (UTC).
See https://pubs.acs.org/sharingguidelines for options on how to legitimately share published articles.

ACS Publications © 2020 American Chemical Society

of the band gaps of Si (1.1 eV as mentioned elsewhere) and bulk MoS_2 (1.3 eV[21]), there would only be ∼0.2 eV to be distributed between the electron and hole barriers at the Si/MoS_2 interface. According to our previous study, the electron barrier is much smaller than the hole barrier.[27] Hence, the CB offset at the Si/MoS_2 interface should be small enough to make MoS_2 an efficient injection barrier in devices like GBTs. Charge transport across vertical "metal/exfoliated-MoS_2/metal" structures has been reported to involve Fowler−Nordheim and thermal injections at high and low electric fields, respectively.[28] However, detailed studies on the vertical transport properties across Si/MoS_2 interfaces are not available. In this work, we experimentally investigate vertical electron transport across vapor-phase-grown layered MoS_2 sandwiched between highly doped silicon and graphene. The Si/MoS_2/graphene heterostructures, which we call semiconductor−semiconductor−graphene (SSG) structures, were fabricated with a scalable process and characterized electrically. These devices are believed to serve as efficient emitter diodes for GBTs. As GBTs operate in the forward-bias regime, where hot electrons from the n^+-Si emitter are injected into the graphene base and then to the collector, the focus of this work is the investigation of the electron transport in the forward-bias regime. The charge carrier transport mechanism is explained through calculations and analyses based on the measured data. Furthermore, electron barrier height values were determined using two different methods: (1) from thermal activation plots and (2) by fitting voltage-dependent barrier heights to the current−voltage (I−V) characteristics measured at different temperatures.

II. EXPERIMENTS AND MODELING

II-A. Device Fabrication. The SSG heterostructures were fabricated as follows: first, Si active areas of various sizes were defined on Si(100) wafers through photolithography followed by Si etching to form trenches. The trenches were then filled with thick silicon oxide (SiO_2) layer deposited by the high-density plasma chemical vapor deposition (CVD) technique. The SiO_2 layer serves as a shallow trench isolation that separates neighboring devices and also helps to avoid direct leakage paths from the metal pads to the underlying Si. After SiO_2 deposition, chemical mechanical polishing was employed to planarize the wafer surface. Then, to create locally doped n^+-Si active regions, phosphorous ion implantation was carried out using silicon nitride as a hard mask. After dicing the wafers into small chips (1.5 cm × 1.5 cm) and performing a standard cleaning procedure, photolithography was used to define larger windows covering the Si active areas. Then, native oxide was removed from the active areas using a 7:1 buffered oxide etch solution, followed by deposition of ∼5 nm molybdenum (Mo) films using an e-beam evaporation. After a liftoff process to complete the Mo film patterning, a thermally assisted conversion of the Mo films was carried out at a temperature of 800 °C inside a CVD furnace in a sulfur atmosphere. This process resulted in ∼15 nm MoS_2 films, as confirmed by atomic force microscopy (AFM) inspections (Figure S2 in the Supporting Information). Also, transmission electron microscopy (TEM) investigations were carried out to inspect the structural formation of the MoS_2 film. The resulting TEM cross-sectional image and the corresponding electron diffraction pattern indicate the polycrystalline nature of the film (Figure S3 in the Supporting Information). Next, a CVD-grown single-layer graphene (SLG) was transferred onto the Si/MoS_2 target samples using a polymer-assisted wet chemical etching transfer technique.[29,30] Afterward, the SLG was patterned using a step of photolithography followed by reactive ion etching in oxygen plasma. Then, metal contacts were formed at two ends of the SLG through a sequence of photolithography, evaporation of 20/120 nm chromium/gold (Cr/Au) stack, and liftoff processes. Finally, the device fabrication was concluded by depositing Cr/Au metal back-contacts to the Si substrates. Schematics of the isometric view of the SSG device are presented in Figure 1a,b. In addition, a top-view

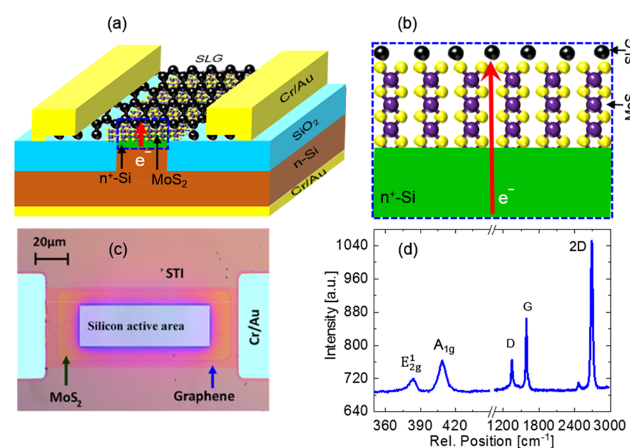

Figure 1. (a) Schematic of an isometric view of the as-fabricated SSG structure, where MoS_2 is used as an emission barrier (the red vertical arrow indicates the electron transport direction). (b) Magnified view of the SSG heterojunction in the active region marked by the blue dashed box in (a). (c) Optical micrograph of the top view of the actual SSG device. (d) Raman spectrum of the MoS_2 and single-layer graphene. The $E_{2g}{}^1$ and $A_g{}^1$ peaks indicate the MoS_2 phase formation, whereas an intense 2D band with 2D/G intensity ratio > 1 confirms the presence of a single-layer graphene of reasonable quality.

optical micrograph of the as-fabricated device is shown in Figure 1c. To inspect the presence and quality of the MoS_2 and SLG layers, Raman spectroscopy was performed on the samples, and the corresponding Raman spectra are presented in Figure 1d, confirming a 2H-MoS_2 phase formation and the monolayer nature of the graphene.

II-B. Modeling Thermionic Emission (TE) across Small Electron Barriers. The early understanding of thermionic emission of charge carriers from solid-state materials began in the 1930s during the development of vacuum tube electronics. Later in 1949, Herring and Nichols summarized the basic formulation of a theory describing the flow of electrons from metals into vacuum.[31] With some refinements over the years, the theory is still being used to describe thermionic emission between metals and semiconductors.[32−37] In the former case, the electron needs to overcome a barrier constituted by the metal work function, which allows to assume isotropic electronic properties, parabolic energy bands, and thus Maxwellian velocity distributions of electrons on both sides of the barrier. For a metal/silicon Schottky structure, a similar assumption can be adopted for the metal, while ellipsoidal constant energy surfaces need to be considered for the silicon CB.[38] This is required to maintain the Maxwellian velocity distribution of charge carriers as a basis for the description of thermionic emission.

In this paper, we investigate electron transport from a highly doped Si into 15 nm layered MoS_2 by assuming a Maxwellian distribution of electrons in the Si passing over a voltage- and temperature-dependent barrier Φ_B that varies from ∼0.3 eV down to 0 eV. Schematic diagrams illustrating the charge distribution in the present system and the associated band alignments are shown in Figure 2. If the right-hand side of the Si/MoS_2 barrier geometry in Figure 2 were vacuum, the electrons from Si would continue into a new isotropic and parabolic energy band. However, in the present sample, they enter an indirect gap polycrystalline MoS_2 with more than one possible CB.[36,37,39] During the charge carrier transfer process, electrons with velocity components in the x direction and energy larger than Φ_B are injected into the MoS_2 layer. At high voltages, Φ_B approaches values lower than the 3 kT limit, below which the Boltzmann statistics is not valid. Therefore, Fermi statistics is needed to be used in our

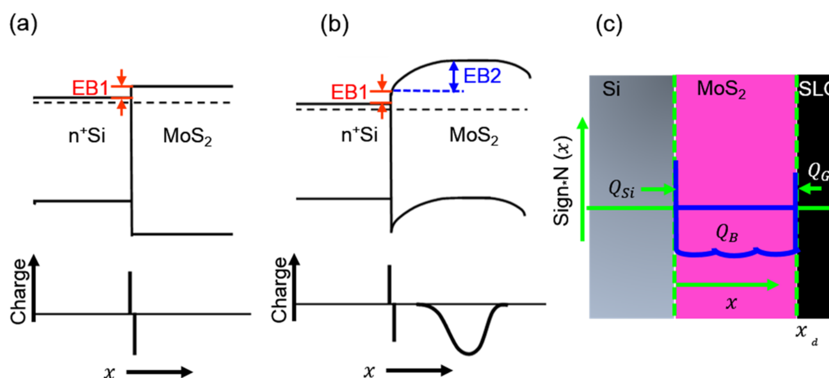

Figure 2. Schematic diagram illustrating the geometrical representation of the Si−MoS_2 band alignment at thermal equilibrium and the associated charge distribution for (a) a neutral MoS_2 layer and (b) MoS_2 with negative charge in its bulk. (c) Schematic diagram for a simple demonstration of the charge distribution in the SSG structure.

calculations to obtain more reliable current data. The injected current is considered proportional to the product $f(E)g(E)$ of the Fermi function, $f(E)$, and the density of states, $g(E)$, integrated along energy, E, of the Si CB from the barrier energy value up to infinity. Hence, the current density, J, becomes

$$J = BT\int_{\Phi_B}^{\infty}\left[\frac{E^{1/2}}{1+\exp\left(\frac{E-E_F}{kT}\right)}\right]dE \tag{1}$$

where B is a constant, E_F is the Fermi level of Si, k is the Boltzmann constant, and T is the temperature. The solution of the integral in eq 1 gives rise to an additional prefactor T such that J becomes proportional to T^2. The assumption, which eq 1 is based on, requires that the electron transmission probability is independent of electron energy and that the two materials have similar density of states as a function of energy.

The Fermi level of the Si emitter is close to the CB edge due to the high doping level, and that makes it possible to treat the structure similar to a Schottky diode. Therefore, for Φ_B larger than about 3 kT, the standard Schottky diode equation, $J = A^*T^2\exp\left(\frac{-\Phi_B}{kT}\right)\left[\exp\left(\frac{-qV}{kT}\right)-1\right]$, can be used to determine the current density. However, the factor $\left[\exp\left(\frac{-qV}{kT}\right)-1\right]$ approaches a value of −1 for voltages used in the present case, as small as −0.1 V. Hence, the full diode equation is simplified to a version similar to the Richardson expression given by[34,35]

$$J = A^*T^2\exp\left(\frac{-\Phi_B}{kT}\right) \tag{2}$$

where A^* is a pre-exponential coefficient known as the effective Richardson constant.

As will be demonstrated later in the Results and Discussion section, the heterojunction barrier in the present case has both temperature and bias dependence that can be described as

$$\Phi_B(V, T) = \Phi_{B0}(V) + \alpha(V, T)T \tag{3}$$

where $\alpha(V,T)$ is a proportionality factor and $\Phi_{B0}(V)$ is the bias-dependent barrier height at T = 0 K, provided that α is temperature-independent. Combining the Richardson expression in eq 2 with eq 3, one can get

$$\frac{J}{T^2} = A^*\exp\left[-\left(\frac{\alpha(V)}{k} + \Phi_{B0}(V)\frac{1}{kT}\right)\right] \tag{4}$$

Hence, an Arrhenius plot of $\ln\left(\frac{J}{T^2}\right)$ vs $\frac{1}{kT}$ would give a slope determined by Φ_{B0}.

II-C. Influence of Charge on the MoS_2 Band Diagram. In the present structure, a small electron barrier (i.e., <100 meV) forms at the Si/MoS_2 interface at thermal equilibrium. Hence, electrons injected from the Si into MoS_2 face this low-energy barrier (EB1), provided that the MoS_2 layer is neutral (Figure 2a). However, as was found in our earlier work,[27] negative charge exists inside the MoS_2 bulk that influences the shape of the MoS_2 CB by inducing an additional barrier (EB2) for electrons (Figure 2b). This moves the barrier maximum from the interface to a point on the CB edge on the MoS_2 layer. The influence of the aforementioned charge on the electron barrier can be modeled using the Poisson equation. To maintain charge conservation, the net charge in the Si/MoS_2/graphene (Gr) structure should be zero. This implies that the MoS_2 bulk charge, $Q_B(x)$, is compensated by charges at the Si/MoS_2 and MoS_2/Gr interfaces, as illustrated by the schematic diagram in Figure 2c. If the charge at the Si/MoS_2 interface, Q_{Si}, is a fraction, a, of the total bulk charge, Q_B, so that

$$Q_{Si} = aQ_B(x) \tag{5}$$

then the charge at the MoS_2/Gr interface would be

$$Q_{Gr} = (1-a)Q_B(x) \tag{6}$$

where x is the distance from the Si interface into the MoS_2 bulk. For an arbitrary depth distribution, $N(x)$, of negative charges inside MoS_2, the total bulk charge would be

$$Q_B(x) = -q\int_0^{x_d} N(x)dx \tag{7}$$

where the minus sign is due to the negative bulk charge in the present case, and x_d is the maximum distance from the Si/MoS_2 interface. For a known depth distribution of the bulk charge, eqs 5−7 can be used to derive an expression for the electric field, $F(x)$, as

$$F(x) = \frac{1}{\varepsilon\varepsilon_0}(Q_B(x) + Q_{Si}) + \frac{(\Phi_{Gr}-\Phi_{Si})}{x_d} \tag{8}$$

where ε_0 is the permittivity of vacuum, ε is the electronic dielectric constant of MoS_2, and Φ_{Gr} and Φ_{Si} are the work functions of graphene and Si, respectively. Once the electric field is obtained using eq 8, the bending of the MoS_2 CB, E_C[eV] can be calculated using the expression

$$E_C(x) = \int_0^{x_d} F(x)dx \tag{9}$$

Accounting for the effect of image force barrier lowering due to image charges building up in the Si as electrons leave, eq 9 can be rewritten as

$$E_C(x) = \int_0^{x_d} F(x)dx - \frac{q}{16\pi\varepsilon\varepsilon_0}\left(\frac{1}{x}\right) \tag{10}$$

https://dx.doi.org/10.1021/acsami.9b21691
ACS Appl. Mater. Interfaces 2020, 12, 9656−9663

For the $E_C(x)$ calculations, an electronic dielectric constant value of ε_i = 3 was used with the following considerations. A large concentration of electrons with lower thermal energies are injected into MoS_2 at higher voltages due to the lowering of the barrier maximum (EB2). This gives rise to a lower electron velocity in the MoS_2 crystal. As the dielectric constant depends on carrier velocity, it is possible that the electronic dielectric constant of the MoS_2 in the present case approaches the static value.[27]

III. RESULTS AND DISCUSSION

$I-V$ characterizations were conducted on the final SSG devices in a Lakeshore cryogenic probe station connected to a Keithley 4200SCS parameter analyzer and a Lakeshore 336 temperature controller. During the measurements, the chuck temperature was varied from 200 to 300 K at intervals of 20 K. The device schematic with the associated wiring setup used during the measurements is shown in Figure 3a. Temperature-dependent

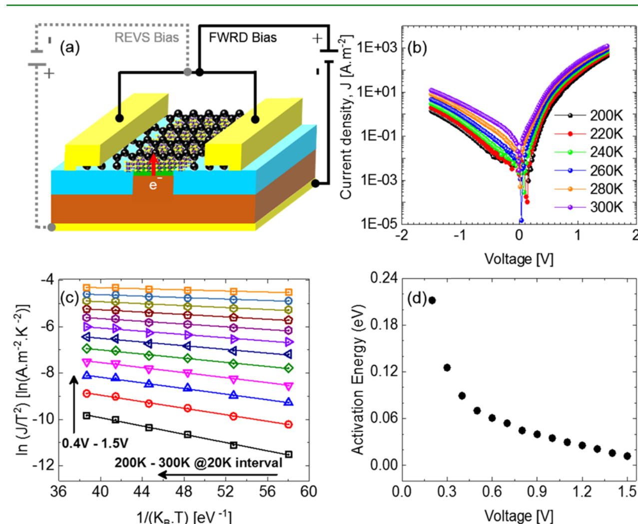

Figure 3. (a) Schematic of isometric view of the SSG structure with a wiring setup used for the $I-V$ measurements. (b) $I-V$ characteristics measured on the SSG devices in vacuum at temperatures ranging from 200 to 300 K with a 20 K interval showing asymmetric and temperature-dependent current with low turn-on voltages (V_{ON}). (c) $\ln[J/T^2]$ vs $(K_BT)^{-1}$, Richardson plots with high linearities indicating a major contribution of thermionic emission to the overall current across the SSG devices. (d) Activation energy, E_a, versus forward-bias voltage V from which the zero-bias heterojunction barrier height, Φ_{B0}, value is extracted.

$I-V$ measurements are presented in Figure 3b as current density versus voltage ($J-V$) plots. The graphs exhibit considerable temperature dependence in both positive and negative branches, indicating thermally assisted transfer of charge carriers. The $J-V$ plots also show a clear asymmetry, that is, a diode behavior with a high slope and a very small voltage at the lowest current levels. The observed rectification behavior can be attributed to the asymmetric electron barriers present at the Si/MoS_2 junction during the forward-bias condition and at the SLG/MoS_2 junction during the reverse-biased condition. We have also checked if the SLG/MoS_2 junction has an influence on the forward-bias current conduction using analytical simulations. The results have verified that no electron barrier actually exists at that junction in the forward-bias condition (Figure S4, in the Supporting Information). In addition, the current scales with device size (Figure S5, in the Supporting Information). A comparison of the room-temperature $I-V$ characteristics of the present devices with the corresponding results from "graphene/n-Si" Schottky diodes intensively studied by our research group[40−44] clearly indicates the electrical impact of MoS_2 in the present structures. Unlike the results in the present work, the $I-V$ characteristics of the graphene/n-Si Schottky diodes in those reports consistently show a nearly flat reverse-biased dark current with higher rectification.

The measured forward-bias $I-V$ data were analyzed using the classic current transport models in semiconductor physics. In this regard, Fowler−Nordheim tunneling (FNT),[32] direct tunneling (DT),[45,46] space-charge-limited transport (SCL),[32] trap-assisted tunneling (TAT),[47] and thermionic emission (TE)[32] were examined for correlations with the experimental data. The strong temperature dependence that is evident from the measured $J-V$ characteristics (Figure 3b) rules out FNT and DT, as both conduction mechanisms should not exhibit temperature dependence. Moreover, the MoS_2 layer is thick enough (∼15 nm) to suppress DT.[46] Besides FNT and DT, SCL is also ruled out due to the lack of a V^2 dependence in the current.[48] This was verified by analyzing the data using the FNT, DT, and TAT models (not shown here) from which no correlations were found. This leaves TE as the most probable transport mechanism for current conduction across the SSG heterostructures. According to the conventional TE model (eq 2), plots of "$\ln(J/T^2)$ versus $1/(k_BT)$" at given biases are expected to yield linear curves with negative slopes. The measured $J-V$ data were replotted in this form, resulting in a set of Richardson plots (Figure 3c). The linearities observed in these plots strongly support that current conduction across the SSG heterostructures is mainly due to thermally stimulated transfer of charge carriers. The heterojunction emission barrier height was extracted from both the Richardson plot and modeled $I-V$ characteristics. The slope of each Richardson plot provides the respective activation energy, which in the current case corresponds to the heterojunction barrier height at 0 K, Φ_{B0} (V), for a temperature-independent α. To demonstrate how $\Phi_{B0}(V)$ reacts to bias, the extracted activation energies are plotted as a function of voltage in Figure 3d, where a decrease in Φ_{B0} is exhibited for increasing bias. This behavior is a clear manifestation of a bias-dependent barrier lowering, which is an essential part of the TE mechanism. The effective Richardson constant values were also extracted from the intercepts of Figure 3c and were found to be bias-dependent with values ranging from 30 A cm^{-2} K^{-2} at 0.4 V to 120 A cm^{-2} K^{-2} at 0.9 V. This effect can be attributed to the bias-dependent proportionality factor, α, given in eqs 3 and 4. By combining eqs 2 and 4, it can be shown that the measured effective Richardson constant from eq 4, which we call now A^*_m, becomes a function of α such that $A^*_m = A^* \exp(-\alpha/k)$. Since eq 2 is not valid for barrier values smaller than 3 kT, as emphasized in Modeling Thermionic Emission (TE) across Small Electron Barriers section, and the A^*_m values are calculated using this equation, the resulting A^*_m values for voltages above ∼0.9 V are not valid for the present system. Above this voltage, the barrier Φ_B crosses the 3 kT limit, below which eq 1 will govern the system instead of eq 2. As a demonstration of how the TE transport mechanism operates in the SSG structure, illustrative band diagrams are shown in Figure 4a,b for thermal equilibrium and forward-bias conditions, respectively.

The barrier heights were also obtained by modeling. The schematics in Figure 5a,b demonstrate the charge carrier

https://dx.doi.org/10.1021/acsami.9b21691
ACS Appl. Mater. Interfaces 2020, 12, 9656−9663

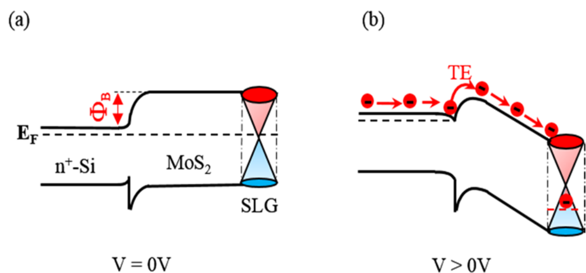

Figure 4. Schematics of band diagrams of an SSG structure in (a) thermal equilibrium and (b) forward-bias conditions with illustrations of the electron transfer process from Si to MoS_2 via thermionic emission (TE).

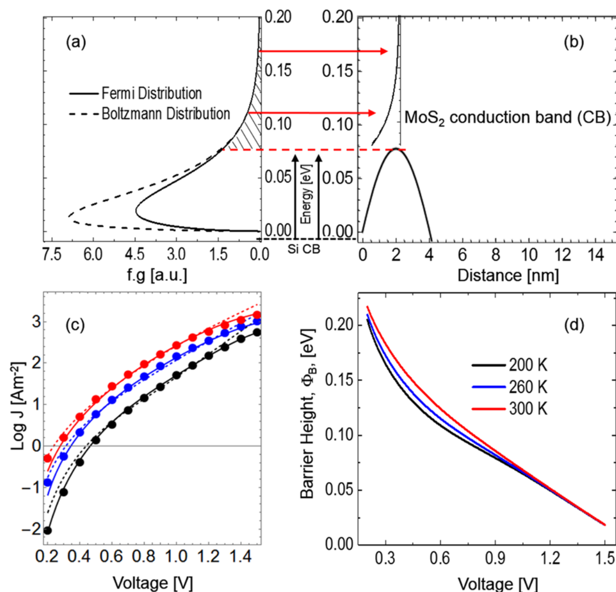

Figure 5. Boltzmann versus Fermi–Dirac statistics for low-energy barriers: (a) "f.g vs *E*" graph showing distribution of carriers at the Si CB edge. (b) Graph illustrating the MoS_2 CB bending as a function of distance into the MoS_2 depth. The schematic on top of the highest potential (EB2) is the Fermi tail of distribution of electron states in the MoS_2, resembling that of Si at similar energy values. The horizontal red arrows illustrate the transfer of electrons from Si to MoS_2, while the dashed line marks the barrier maximum to indicate that only electrons having energies above this line will be injected into MoS_2. The hatched region shows the concentration of electrons that can be injected into MoS_2. (c) Comparison of measured *I*–*V* (dots) and simulated *I*–*V* (lines) for 200 K (black), 260 K (blue), and 300 K (red) measurement temperatures. The solid *I*–*V* curves in (c) are calculated using Fermi distribution, while the dashed ones are based on Boltzmann distribution. (d) Comparison of barrier functions used to calculate *I*–*V* curves and fit them to the measured data at different temperatures as shown in (c). The barrier curves are seen to merge for $V \geq 1$ V.

transfer in which thermally excited electrons leave the Si crystal and escape over the energy barrier at the Si/MoS_2 interface. The electron energy distributions in both materials are also illustrated in the schematics. To calculate the *I*–*V* characteristics, it was assumed that the ballistic part of the electron transport from Si into the MoS_2 CB maximum is proportional to the total concentration of electrons in the energy range above the barrier maximum (i.e., hatched area in Figure 5a). Ballistic transport is generally used for transport without scattering. In a more rigorous treatment, one would take scattering processes into account. However, such attempts can be done only more information about the interface than what is available for the present system. Based on the consistency of the data shown in the present work, we believe that the approximation used here is adequate. The energy distribution of electrons heading toward the barrier is given by the product of the Fermi function and the density of states in the Si parabolic CB, which is proportional to $(E - E_F)^{1/2}$ for a Maxwellian electron gas. The *I*–*V* characteristics were then calculated for 200 K (black), 260 K (blue), and 300 K (red), using a model (eq 1) analogous to the reasoning in ref 49 and fitted to the corresponding experimental data using bias-dependent barrier height functions as fitting parameters (Figure 5c). The solid and dotted curves in this figure represent *I*–*V* characteristics calculated using Fermi and Boltzmann distributions, respectively. The Fermi distribution fits the measured data better than the Boltzmann distribution, especially in the higher bias range. As depicted in Figure 5d, different "Φ_B vs V" curves (black, blue, and red) were needed to reproduce the measured *I*–*V* characteristics at 200, 260, and 300 K, respectively. A maximum difference of ~45 meV is noted at about 0.4 V between the shapes of the barrier curves, which eventually merge for $V \geq \sim 1$ V.

As described in the Experiments and Modeling Sction, the negative charge accommodated within the MoS_2 layer influences the shape of its CB, and thereby limits the current across the SSG heterostructures. Assuming a Gaussian depth distribution of this charge as shown in Figure 6a, the electric field, $F(x)$, was calculated for various voltage values using eq 8. The MoS_2 CB, E_C, was then calculated from the resulting $F(x)$

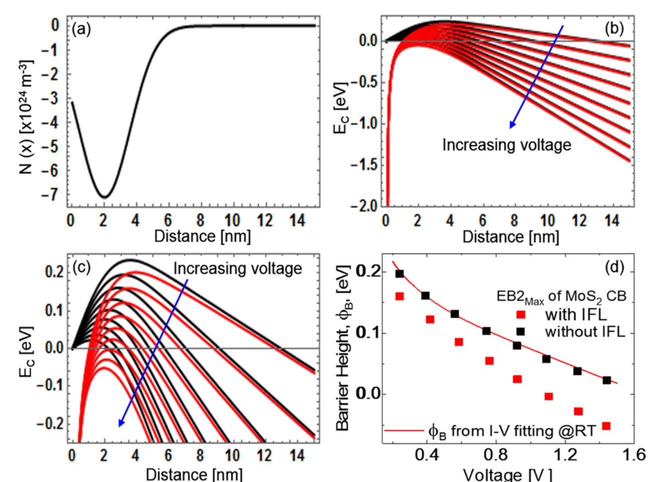

Figure 6. (a) Gaussian distribution of negative charges inside the MoS_2 bulk. (b) MoS_2 CB bending as a function of voltage across the layer depicting the formation of the electron barrier EB2, which is determined by the negative charge in the bulk. (c) Magnified version of the graph in (b) along the vertical axis for better visibility of the CB maxima in determining the value of $EB2_{Max}$ at different voltages. (d) Comparison of the maxima of the potential barrier plots in (c) (symbols) and the barrier function used to fit the calculated *I*–*V* with the measured data at 300 K (red solid curve) entailing that the charge-induced barrier (EB2) determines the current across the present structures. The red and black curves and points represent calculations with and without consideration, respectively, of the effect of image force barrier lowering (IFL). The parameters used to calculate the MoS_2 CB are: x_d = 15 nm, Q_B (concentration of charge in the MoS_2 bulk) = -7.097×10^{24} m^{-3}, ε = 3, and $\Phi_G - \Phi_{Si}$ = ~0.45 eV.

https://dx.doi.org/10.1021/acsami.9b21691
ACS Appl. Mater. Interfaces 2020, 12, 9656–9663

values using eq 9. The black curves in Figure 6b,c show the calculated MoS_2 CB demonstrating a band bending that increases with increasing bias. To account for the effect of image force lowering on the MoS_2 CB bending, calculations were also done using eq 10, which includes Schottky lowering. The resulting CB bending curves are presented as the red curves in Figure 6b,c. The maximum points of the CB curves were extracted from Figure 6c and compared to the barrier function obtained by fitting the calculated $I-V$ to the measured data at room temperature. Figure 6d presents a comparison in which the barrier data without image force lowering (black points) fit well, while the corresponding data with image force lowering (red points) do not.

The heterojunction barrier heights extracted using Richardson's analysis from activation energies (Figure 3c) and those obtained by calculating $I-V$ curves and fitting them to the measured data (Figure 5c) lead to different results: the values obtained from thermal activation data (Figure 3d) are considerably smaller than those obtained from $I-V$ fitting (Figure 5d). This aspect requires further discussion. At barrier heights larger than $\sim 3\ kT$, the Fermi distribution can be approximated by the Boltzmann distribution to obtain the Richardson expression (eq 2). However, as shown in Figure 5a, the Boltzmann distribution assumes a larger electron concentration than actually is available at very low energy barriers and thus overestimates the current. Therefore, this approximation would be in jeopardy for barriers lower than $\sim 3\ kT$, which corresponds to the red dashed line in Figure 5a,b. As depicted in Figure 5c, the calculated current based on Boltzmann distribution diverges from the measured data at high voltages, while the data established by the Fermi distribution show a better agreement. The discrepancy between the current calculated using the Boltzmann distribution and the measured data for $V < 0.4$ V might originate from the assumption on the electron transition probability and density of states, as pointed out in the Experiments and Modeling Section.

Approximating the Gaussian distribution of the MoS_2 charge (Figure 6a) by a sheet charge and multiplying its full width at half-maximum by its amplitude, one would obtain a concentration of about $2.8 \times 10^{16}\ m^{-2}$. Moving this charge between the Si/graphene and Si/MoS_2 interfaces would introduce a voltage variation of ~ 1.4 V across the MoS_2 layer. This is in the range of the flat-band voltage (V_{FB}) shift due to the negative charges in the MoS_2 bulk as observed in our earlier work.[27,50,51] It is worth noting here that, for a nonhomogeneous charge distribution across the SSG structure (Figure 2c), the electric field at the Si/MoS_2 interface differs considerably from V/d. As demonstrated in Figure 6b,c, the negative charges in MoS_2 induce a barrier (EB2) whose maximum point gradually shifts toward the Si/MoS_2 interface for increasing applied voltage. The height of this barrier also decreases with increasing voltage and eventually disappears as can be noted from the figures. As electrons leave Si and approach the Si/MoS_2 interface, they may experience an attraction force from the image charges that build up in the Si. An image force associated with these charges can slightly lower the effective height of the heterojunction barrier (EB2), and the lowering may increase with increasing bias as demonstrated by the red curves in Figure 6b,c. However, the comparison in Figure 6d asserts that the charge-induced barrier (EB2) dominates the interface barrier (EB1) and determines the current conduction across the SSG structure. Also, this result ratifies that the image force lowering may not be applicable to the present case.[52]

From the differences exhibited among the barrier height values obtained by modeling the $I-V$ data at different temperatures (Figure 7a,b), we found that the heterojunction

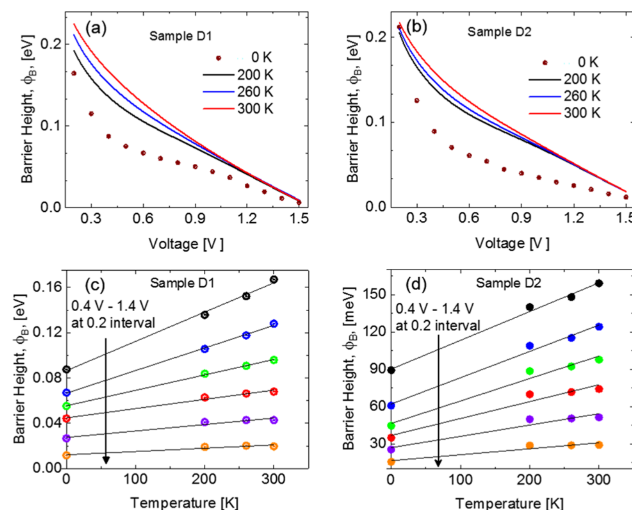

Figure 7. Comparison of barrier height values extracted from activation plots (symbols) with barrier height functions used to fit the measured $I-V$ curves at 200 K (black), 260 K (blue) and 300 K (red) for (a) sample D1 and (b) sample D2. Barrier height, Φ_B, as a function of temperature, T, at different voltages for (c) sample D1 and (d) sample D2 showing a linear dependence of Φ_B on temperature.

barrier height, Φ_B, is temperature-dependent. As shown in Figure 7c,d, Φ_B has a nearly linear temperature dependence that can be formulated using a first-order approximation as in eq 3. The proportionality factor α in eq 3 could be related to the change in entropy taking place in the electron ensemble during its transfer from Si to MoS_2. According to eqs 3 and 4, barrier height values obtained from activation plots based on the conventional Richardson expression can be identified as Φ_{B0}, which corresponds to the intercepts of the $\Phi_B(T)$ vs T plots shown in Figure 7c,d. Other possibilities to explain the temperature dependence of the barrier height could be one or more of the following: change in the difference between the band gaps of Si and MoS_2, strain at the Si/MoS_2 interface, and/or barrier inhomogeneity across the sample area. Also, as reported in previous works, strain influences the effective mass of electrons in MoS_2,[53] which makes its contribution to the observed temperature dependence under discussion a possibility.

Throughout the discussion in the paper, the overall charge carrier transfer between Si and MoS_2 has been considered unaffected by the interfacial silicon oxide layer lying between the two materials, as revealed by the TEM cross section (Supporting Information Figure S3). This layer is found to be very leaky compared to the standard SiO_2 of similar thickness and bias level,[54] leading to the assumption that it is nearly transparent to electrons under DC bias. This assures that the bottleneck for the current conduction across the SSG structure is the charge carrier injection across the MoS_2 layer.

IV. CONCLUSIONS

Semiconductor−semiconductor−graphene (SSG) vertical heterostructures were investigated with respect to the vertical

https://dx.doi.org/10.1021/acsami.9b21691
ACS Appl. Mater. Interfaces 2020, 12, 9656−9663

current conduction mechanism to assess their potential as the emitter diodes in vertical hot electron transistors. The SSG structures were fabricated using a scalable and CMOS-compatible process. The measured electrical data exhibit asymmetric $I-V$ characteristics with clear temperature dependence. Richardson plots of the measured data confirmed thermionic emission as the main conduction mechanism, which is the desired mechanism for high-performance hot electron transistors. This result was confirmed through analytical modeling of the $I-V$ characteristics. The heterojunction barrier height was extracted by both methods. The value obtained through the former method is considerably smaller than that from the latter. In fact, the heterojunction barrier height was found to have a linear dependence on temperature, and the values obtained from Richardson plots appear to correspond to values at T = 0 K. The presented extraction method and model may serve as a guideline for future experiments on the electronic properties of 2D heterostructures. In particular, the presented data suggest MoS_2 as a thermionic emission barrier material for vertical hot electron transistors.

■ ASSOCIATED CONTENT

Supporting Information

The Supporting Information is available free of charge at https://pubs.acs.org/doi/10.1021/acsami.9b21691.

Illustrative schematic diagrams showing the structure and operation principle of a graphene base hot electron transistor (GBT), in which the SSG device demonstrated in this paper is used as the active emitter diode (Figure S1); AFM investigation on the as-grown MoS_2 film showing the actual thickness of the MoS_2 film after grown (Figure S2); TEM investigation of MoS_2 revealing the polycrystalline nature of the film (Figure S3); analytical simulation demonstrating the MoS_2 conduction band energy variation, E_C, as a function of distance from the Si/MoS_2 interface for two different values of applied voltage (Figure S4); a brief discussion on the area scaling of the measured $I-V$ characteristics and the corresponding result (Figure S5) (PDF)

■ AUTHOR INFORMATION

Corresponding Authors

Satender Kataria − *Faculty of Electrical Engineering and Information Technology, Chair of Electronic Devices, RWTH Aachen University, 52074 Aachen, Germany;* orcid.org/0000-0003-2573-250X; Email: satender.kataria@eld.rwth-aachen.de

Max C. Lemme − *Faculty of Electrical Engineering and Information Technology, Chair of Electronic Devices, RWTH Aachen University, 52074 Aachen, Germany; AMO GmbH, 52074 Aachen, Germany;* orcid.org/0000-0003-4552-2411; Email: lemme@amo.de

Authors

Melkamu Belete − *Faculty of Electrical Engineering and Information Technology, Chair of Electronic Devices, RWTH Aachen University, 52074 Aachen, Germany*

Olof Engström − *AMO GmbH, 52074 Aachen, Germany*

Sam Vaziri − *Department of Electrical Engineering, Stanford University, Stanford, California 94305, United States;* orcid.org/0000-0003-1234-6060

Gunther Lippert − *IHP—Leibniz-Institut für innovative Mikroelektronik, 15236 Frankfurt, Germany*

Mindaugas Lukosius − *IHP—Leibniz-Institut für innovative Mikroelektronik, 15236 Frankfurt, Germany;* orcid.org/0000-0002-5089-348X

Complete contact information is available at: https://pubs.acs.org/10.1021/acsami.9b21691

Notes

The authors declare no competing financial interest.

■ ACKNOWLEDGMENTS

The authors thank Gregor Schulte from the University of Siegen for his kind help in the deposition of initial molybdenum films. The authors are also thankful to Prof. Joachim Mayer and Maximilian Kruth for TEM imaging. Financial support from the European Commission (Graphene Flagship, 785219, QUEFORMAL, 829035) the German Ministry of Education and Research, BMBF (GIMMIK, 03XP0210, NeuroTec, 16ES1134), and the German Research Foundation, DFG (MOSTFLEX, 407080863) is gratefully acknowledged.

■ REFERENCES

(1) Mead, C. A. Operation of Tunnel-Emission Devices. *J. Appl. Phys.* **1961**, *32*, 646−652.

(2) Mehr, W.; Dabrowski, J.; Scheytt, J. C.; Lippert, G.; Xie, Y.; Lemme, M. C.; Ostling, M.; Lupina, G. Vertical Graphene Base Transistor. *IEEE Electron Device Lett.* **2012**, *33*, 691−693.

(3) Vaziri, S.; Lupina, G.; Henkel, C.; Smith, A. D.; Östling, M.; Dabrowski, J.; Lippert, G.; Mehr, W.; Lemme, M. C. A Graphene-Based Hot Electron Transistor. *Nano Lett.* **2013**, *13*, 1435−1439.

(4) Zeng, C.; Song, E. B.; Wang, M.; Lee, S.; Torres, C. M.; Tang, J.; Weiller, B. H.; Wang, K. L. Vertical Graphene-Base Hot-Electron Transistor. *Nano Lett.* **2013**, *13*, 2370−2375.

(5) Lemme, M. C.; Li, L.-J.; Palacios, T.; Schwierz, F. Two-Dimensional Materials for Electronic Applications. *MRS Bull.* **2014**, *39*, 711−718.

(6) Vaziri, S.; Belete, M.; Litta, E. D.; Smith, A. D.; Lupina, G.; Lemme, M. C.; Östling, M. Bilayer Insulator Tunnel Barriers for Graphene-Based Vertical Hot-Electron Transistors. *Nanoscale* **2015**, *7*, 13096−13104.

(7) Torres, C. M.; Lan, Y.-W.; Zeng, C.; Chen, J.-H.; Kou, X.; Navabi, A.; Tang, J.; Montazeri, M.; Adleman, J. R.; Lerner, M. B.; et al. High-Current Gain Two-Dimensional MoS_2-Base Hot-Electron Transistors. *Nano Lett.* **2015**, *15*, 7905−7912.

(8) Vaziri, S.; Smith, A. D.; Östling, M.; Lupina, G.; Dabrowski, J.; Lippert, G.; Driussi, F.; Venica, S.; Di Lecce, V.; Gnudi, A.; et al. Going Ballistic: Graphene Hot Electron Transistors. *Solid State Commun.* **2015**, *224*, 64−75.

(9) Zubair, A.; Nourbakhsh, A.; Hong, J.-Y.; Qi, M.; Song, Y.; Jena, D.; Kong, J.; Dresselhaus, M.; Palacios, T. Hot Electron Transistor with van Der Waals Base-Collector Heterojunction and High-Performance GaN Emitter. *Nano Lett.* **2017**, *17*, 3089−3096.

(10) Guo, H.; Li, L.; Liu, W.; Sun, Y.; Xu, L.; Ali, A.; Liu, Y.; Wu, C.; Shehzad, K.; Yin, W. Y.; et al. All-Two-Dimensional-Material Hot Electron Transistor. *IEEE Electron Device Lett.* **2018**, *39*, 634−637.

(11) Di Lecce, V.; Grassi, R.; Gnudi, A.; Gnani, E.; Reggiani, S.; Baccarani, G. Graphene-Base Heterojunction Transistor: An Attractive Device for Terahertz Operation. *IEEE Trans. Electron Devices* **2013**, *60*, 4263−4268.

(12) Venica, S.; Driussi, F.; Palestri, P.; Esseni, D.; Vaziri, S.; Selmi, L. Simulation of DC and RF Performance of the Graphene Base Transistor. *IEEE Trans. Electron Devices* **2014**, *61*, 2570−2576.

(13) Di Lecce, V.; Grassi, R.; Gnudi, A.; Gnani, E.; Reggiani, S.; Baccarani, G. Graphene Base Transistors: A Simulation Study of DC

and Small-Signal Operation. *IEEE Trans. Electron Devices* **2013**, *60*, 3584−3591.
(14) Alvarado Chavarin, C.; Strobel, C.; Kitzmann, J.; Di Bartolomeo, A.; Lukosius, M.; Albert, M.; Bartha, J. W.; Wenger, C. Current Modulation of a Heterojunction Structure by an Ultra-Thin Graphene Base Electrode. *Materials* **2018**, *11*, 345.
(15) Heiblum, M. Tunneling Hot Electron Transfer Amplifiers (Theta): Amplifiers Operating up to the Infrared. *Solid-State Electron.* **1981**, *24*, 343−366.
(16) Heiblum, M.; Thomas, D. C.; Knoedler, C. M.; Nathan, M. I. Tunneling Hot-electron Transfer Amplifier: A Hot-electron GaAs Device with Current Gain. *Appl. Phys. Lett.* **1985**, *47*, 1105−1107.
(17) Wang, Q. H.; Kalantar-Zadeh, K.; Kis, A.; Coleman, J. N.; Strano, M. S. Electronics and Optoelectronics of Two-Dimensional Transition Metal Dichalcogenides. *Nat. Nanotechnol.* **2012**, *7*, 699−712.
(18) Jariwala, D.; Sangwan, V. K.; Lauhon, L. J.; Marks, T. J.; Hersam, M. C. Emerging Device Applications for Semiconducting Two-Dimensional Transition Metal Dichalcogenides. *ACS Nano* **2014**, *8*, 1102−1120.
(19) Fontana, M.; Deppe, T.; Boyd, A. K.; Rinzan, M.; Liu, A. Y.; Paranjape, M.; Barbara, P. Electron-Hole Transport and Photovoltaic Effect in Gated MoS_2 Schottky Junctions. *Sci. Rep.* **2013**, *3*, No. 1634.
(20) Akinwande, D.; Petrone, N.; Hone, J. Two-Dimensional Flexible Nanoelectronics. *Nat. Commun.* **2014**, *5*, No. 5678.
(21) Mak, K. F.; Lee, C.; Hone, J.; Shan, J.; Heinz, T. F. Atomically Thin MoS_2: A New Direct-Gap Semiconductor. *Phys. Rev. Lett.* **2010**, *105*, No. 136805.
(22) Radisavljevic, B.; Radenovic, A.; Brivio, J.; Giacometti, V.; Kis, A. Single-Layer MoS 2 Transistors. *Nat. Nanotechnol.* **2011**, *6*, 147−150.
(23) Yim, C.; O'Brien, M.; McEvoy, N.; Riazimehr, S.; Schäfer-Eberwein, H.; Bablich, A.; Pawar, R.; Iannaccone, G.; Downing, C.; Fiori, G.; et al. Heterojunction Hybrid Devices from Vapor Phase Grown MoS_2. *Sci. Rep.* **2014**, *4*, No. 5458.
(24) Ryou, J.; Kim, Y.-S.; Kc, S.; Cho, K. Monolayer MoS_2 Bandgap Modulation by Dielectric Environments and Tunable Bandgap Transistors. *Sci. Rep.* **2016**, *6*, No. 29184.
(25) Gong, C.; Zhang, H.; Wang, W.; Colombo, L.; Wallace, R. M.; Cho, K. Band Alignment of Two-Dimensional Transition Metal Dichalcogenides: Application in Tunnel Field Effect Transistors. *Appl. Phys. Lett.* **2013**, *103*, No. 053513.
(26) Hughes, H. P.; Starnberg, H. I. *Electron Spectroscopies Applied to Low-Dimensional Materials*; Springer: Berlin, 2000.
(27) Belete, M.; Kataria, S.; Koch, U.; Kruth, M.; Engelhard, C.; Mayer, J.; Engström, O.; Lemme, M. C. Dielectric Properties and Ion Transport in Layered MoS2 Grown by Vapor-Phase Sulfurization for Potential Applications in Nanoelectronics. *ACS Appl. Nano Mater.* **2018**, *1*, 6197−6204.
(28) Zhu, Y.; Zhou, R.; Zhang, F.; Appenzeller, J. Vertical Charge Transport through Transition Metal Dichalcogenides—a Quantitative Analysis. *Nanoscale* **2017**, *9*, 19108−19113.
(29) Wagner, S.; Weisenstein, C.; Smith, A. D.; Östling, M.; Kataria, S.; Lemme, M. C. Graphene Transfer Methods for the Fabrication of Membrane-Based NEMS Devices. *Microelectron. Eng.* **2016**, *159*, 108−113.
(30) Neumaier, D.; Pindl, S.; Lemme, M. C. Integrating Graphene into Semiconductor Fabrication Lines. *Nat. Mater.* **2019**, *18*, 525−529.
(31) Herring, C.; Nichols, M. H. Thermionic Emission. *Rev. Mod. Phys.* **1949**, *21*, 185−270.
(32) Sze, S. M. *Physics of Semiconductor Devices*, 3rd ed.; Wiley, 2006.
(33) Blakemore, J. S. Solid State Physics by J. S. Blakemore /core/books/solid-state-physics/50A3861A5268A48C385E-F6E78AF5BBFB, 2018. https://doi.org/10.1017/CBO9781139167871.
(34) Crowell, C. R.; Sze, S. M. Electron-Optical-Phonon Scattering in the Emitter and Collector Barriers of Semiconductor-Metal-Semiconductor Structures. *Solid-State Electron.* **1965**, *8*, 979−990.
(35) Crowell, C. R.; Sze, S. M. Current Transport in Metal-Semiconductor Barriers. *Solid-State Electron.* **1966**, *9*, 1035−1048.
(36) Liu, D.; Guo, Y.; Fang, L.; Robertson, J. Sulfur Vacancies in Monolayer MoS_2 and Its Electrical Contacts. *Appl. Phys. Lett.* **2013**, *103*, No. 183113.
(37) Kuc, A.; Zibouche, N.; Heine, T. Influence of Quantum Confinement on the Electronic Structure of the Transition Metal Sulfide TS_2. *Phys. Rev. B* **2011**, *83*, No. 245213.
(38) Crowell, C. R. The Richardson Constant for Thermionic Emission in Schottky Barrier Diodes. *Solid-State Electron.* **1965**, *8*, 395−399.
(39) Cheiwchanchamnangij, T.; Lambrecht, W. R. L. Quasiparticle Band Structure Calculation of Monolayer, Bilayer, and Bulk MoS_2. *Phys. Rev. B* **2012**, *85*, No. 205302.
(40) Riazimehr, S.; Bablich, A.; Schneider, D.; Kataria, S.; Passi, V.; Yim, C.; Duesberg, G. S.; Lemme, M. C. Spectral Sensitivity of Graphene/Silicon Heterojunction Photodetectors. *Solid-State Electron.* **2016**, *115*, 207−212.
(41) Riazimehr, S.; Kataria, S.; Bornemann, R.; Haring Bolívar, P.; Ruiz, F. J. G.; Engström, O.; Godoy, A.; Lemme, M. C. High Photocurrent in Gated Graphene−Silicon Hybrid Photodiodes. *ACS Photonics* **2017**, *4*, 1506−1514.
(42) Riazimehr, S.; Kataria, S.; Gonzalez-Medina, J. M.; Wagner, S.; Shaygan, M.; Suckow, S.; Ruiz, F. G.; Engström, O.; Godoy, A.; Lemme, M. C. High Responsivity and Quantum Efficiency of Graphene/Silicon Photodiodes Achieved by Interdigitating Schottky and Gated Regions. *ACS Photonics* **2019**, *6*, 107−115.
(43) Di Bartolomeo, A.; Luongo, G.; Giubileo, F.; Funicello, N.; Niu, G.; Schroeder, T.; Lisker, M.; Lupina, G. Hybrid Graphene/Silicon Schottky Photodiode with Intrinsic Gating Effect. *2D Mater.* **2017**, *4*, No. 025075.
(44) Luongo, G.; Giubileo, F.; Genovese, L.; Iemmo, L.; Martucciello, N.; Di Bartolomeo, A. I-V and C-V Characterization of a High-Responsivity Graphene/Silicon Photodiode with Embedded MOS Capacitor. *Nanomaterials* **2017**, *7*, 158.
(45) Choi, C.-H.; Oh, K.-H.; Goo, J.-S.; Yu, Z.; Dutton, R. W. In *Direct Tunneling Current Model for Circuit Simulation*, International Electron Devices Meeting 1999. Technical Digest (Cat. No.99CH36318), 1999; pp 735−738.
(46) Roy, K.; Mukhopadhyay, S.; Mahmoodi-Meimand, H. Leakage Current Mechanisms and Leakage Reduction Techniques in Deep-Submicrometer CMOS Circuits. *Proc. IEEE* **2003**, *91*, 305−327.
(47) Houng, M. P.; Wang, Y. H.; Chang, W. J. Current Transport Mechanism in Trapped Oxides: A Generalized Trap-Assisted Tunneling Model. *J. Appl. Phys.* **1999**, *86*, 1488.
(48) Rose, A. Space-Charge-Limited Currents in Solids. *Phys. Rev.* **1955**, *97*, 1538−1544.
(49) Kim, R.; Jeong, C.; Lundstrom, M. S. On Momentum Conservation and Thermionic Emission Cooling. *J. Appl. Phys.* **2010**, *107*, No. 054502.
(50) Belete, M.; Kataria, S.; Engström, O.; Lemme, M. C. In *Defects in Layered Vapor-Phase Grown MOS_2*, 2017 75th Annual Device Research Conference (DRC), 2017; pp 1−2.
(51) Belete, M.; Kataria, S.; Turfanda, A.; Vaziri, S.; Wahlbrink, T.; Engström, O.; Lemme, M. C. Nonvolatile Resistive Switching in Nanocrystalline Molybdenum Disulfide with Ion-Based Plasticity. *Adv. Electron. Mater.* **2020**, No. 1900892.
(52) Tung, R. T. The Physics and Chemistry of the Schottky Barrier Height. *Appl. Phys. Rev.* **2014**, *1*, No. 011304.
(53) Peelaers, H.; Van de Walle, C. G. Effects of Strain on Band Structure and Effective Masses in MoS_2. *Phys. Rev. B* **2012**, *86*, No. 241401.
(54) Rana, F.; Tiwari, S.; Buchanan, D. A. Self-consistent Modeling of Accumulation Layers and Tunneling Currents through Very Thin Oxides. *Appl. Phys. Lett.* **1996**, *69*, 1104−1106.